Measurements for refractory protection in pyrometallurgical recycling of lithium-ion batteries

Lukas Wiszniewski [a,*] , Zlatko Raonic [a], Irmtraud Marschall [b], Andreas Schönberg [c], Damaris Legenstein [a], Klaus Doschek-Held [a]

[a] Montanuniversität Leoben, Chair of Thermal Processing Technology, Leoben, Austria
[b] K1-MET GmbH, in Cooperation with Montanuniversität Leoben, Chair of Ceramics, Leoben, Austria
[c] Schönberg – Process Engineering Calculations (S-PEC), Graz, Austria

ARTICLE INFO

ABSTRACT

Recycling lithium-ion batteries (LIB) has become a key priority within the European Union's resource strategy, inducing a regulatory framework with ambitious recycling targets. Currently, no recycling technology meets these targets while remaining economically viable. The InduRed reactor, with its innovative pyrometallurgical approach via carbothermic reduction, presents a potential solution. A critical challenge, however, is the crucible's performance in the highly corrosive environment of aggressive melts and reducing gases. To address this, two protective measurements for a magnesium-oxide (MgO) crucible were investigated: one involved applying a thin graphite coating to minimize lithium diffusion, while the other utilized varying sizes of graphite cubes to create a protective temperature gradient. In addition, this study included the simulation of temperature distribution within the crucible using the OpenFOAM multi-region framework as a reason for the high impact of temperature on several different chemical and physical phenomena within the recycling process. Experimental findings show minimal lithium diffusion and corrosion in the graphite-coated crucible, with transfer coefficients above 90 % for all elements and up to 99 % for lithium. As revealed by Micro XRF cross-sectional analysis, the crucible with varying susceptor material sizes showed no contact between the input material and the refractory. This configuration can effectively act as a thermal and physical shield, providing an optimal barrier that prevents corrosion and diffusion effects at the crucible wall. This study demonstrates the potential of combining coatings and varied susceptor sizes for crucible protection, offering promising prospects for the InduRed reactor in future industrial applications.

1. Introduction

The urgency of sustainable solutions in the energy sector has never been more pronounced [1,2], with the surge of lithium-ion batteries (LIB) accentuating the need for efficient recycling technologies [3]. As the demand for electric vehicles and portable electronics has increased drastically in recent years [4], the inevitable end-of-life for these batteries presents both an environmental challenge and a resource opportunity [5]. Recycling LIBs mitigates hazardous waste's environmental impact and recovers valuable materials, reducing the reliance on mining and the associated ecological footprint [6]. The European Union's list of critical raw materials, which includes lithium (Li), phosphorus (P), nickel (Ni), and cobalt (Co), reflects the strategic importance and supply risk associated with these elements [7]. To address these concerns, the EU has introduced the concept of a battery passport and set ambitious recycling quotas, mandating the recovery of 80 % of Li and 95 % of Ni, Co, and copper (Cu) by 2031 [8]. These measures aim to ensure a secure supply of critical materials and foster a circular economy within the battery industry. However, state-of-the-art recycling solutions come with different, severe disadvantages. While toxic gases are released within pyrometallurgical approaches, and Li is most often slagged, hydrometallurgical approaches suffer from vast amounts chemical consumption and correlated wastewater generation [9–12].

Within this context, the InduRed reactor concept emerges as a pivotal innovation in recycling, utilizing carbothermal reduction to recover precious metals from spent batteries [13–15]. The reactor's design consists of a crucible filled with graphite cubes, acting as a susceptor material for an outer magnetic field for inductive heating. The

---

formation of thin melting films or tiny droplets over the graphite cubes favor the extraction of volatile elements like Li and P via the gas stream, while Ni, Co, Fe, and Cu are recovered as an alloy. Aluminum as aluminum-oxide (Al_2O_3) and possible slag formers are retrieved as a separate mineral phase and could be used as secondary raw material for further research on alternative binder components [16]. To fully realize the potential of recycling methods within pyrometallurgy, special attention must be given to the structural materials of the reactor used in the melting operations. Specified, the success of such recycling processes is contingent upon the integrity and performance of crucible materials used in the melting operations [17]. Previous tests within the InduMelt plant have revealed significant shortcomings in using Al_2O_3 and magnesium-oxide (MgO) crucibles, with Al_2O_3 suffering from severe corrosion and the used MgO variant facing issues with Li and P diffusion [18,19]. These challenges necessitate exploring alternative materials or crucible designs that can withstand the harsh conditions of the melting process while preventing contamination of the recovered metals.

Recent experiments by the authors have introduced Silicon Carbide (SiC) and Chromium Oxide (Cr_2O_3) as potential candidates, with SiC demonstrating exceptional results. SiC crucibles exhibit superior resistance to corrosion and minimal metal diffusion, making them a promising solution for the InduMelt plant's operations [20]. Despite these advancements, carbon-based materials remain the gold standard for addressing corrosion and diffusion problems due to their unparalleled inertness, thermal stability, low wettability, and low open porosity [21–23]. Nevertheless, the use of carbon in the InduRed reactor is complicated by its susceptibility to inductive heating, which conflicts with the plant's design that aims to selectively heat only the graphite cubes. To circumvent this issue, two new concepts regarding LIB recycling within the InduMelt reactor have been investigated in this paper.

The first concept involves the application of a thin graphite layer onto a MgO crucible. This approach aims to leverage the beneficial properties of graphite while minimizing its inductive heating by restricting its presence to a mere coating [24]. The second concept utilizes a MgO crucible filled with varying-sized graphite cubes as susceptor material. The geometry of the cubes significantly impacts eddy currents and, thus, the effectiveness of the susceptor's coupling with the magnetic field. The resulting heat generation is based on the field's frequency and geometry, where the relative heat decreases with decreasing volume [25,26]. With reduced temperatures closer to the crucible wall, the melt's viscosity should increase so that the flow behavior is limited and a protective barrier is built. The investigation focuses on whether these design variations positively impact the chemical wear of the crucible and lead to an increased transfer coefficient of Li. The crucible materials were comprehensively analyzed using micro XRF and SEM-EDX to assess corrosion and diffusion. Additionally, Li extraction efficiency was evaluated through ICP-MS and ICP-OES measurements of the different product phases. These analyses aim to provide a detailed understanding of the interactions between crucible design and material performance under high-temperature conditions, ultimately contributing to the optimization of the recycling process. Integrating these crucible designs would mark a significant step forward in the sustainable recycling of critical raw materials within LIBs, aligning with the EU's vision for a resilient and environmentally responsible battery supply chain.

2. Materials & methods

2.1. Lithium-ion battery materials

Previous tests conducted by Holzer et al., 2021 [27] and Wiszniewski et al., 2024 [20] have shown that among different cathode chemistries, $LiCoO_2$ (LCO) tends to be the most aggressive and corrosive chemistry regarding the wear of the refractory material. A synthesized black mass with LCO cathode chemistry was prepared to stress-test new crucible designs with different refractory materials. To replicate the composition of a black mass derived through the recycling process of real-life batteries, a homogenized mixture was synthesized utilizing cathode material sourced from Gelon Energy Corporation, Linyi, China. This cathode material was mixed with a selection of elemental constituents commonly identified within the black mass postulated to originate from the mechanical pre-processing stages, such as thermal pre-treatment and shredding processes. The shredding process introduces metallic contaminants into the black mass, predominantly Al and Cu, which are derived from the current collector foils of the electrodes, as well as Fe sourcing from the protective encasement of the cell. In addition, elemental carbon (C) was added to the mixture to simulate the anode, which is characteristically composed of graphitic material [28]. To ensure experimental consistency and the validity of comparative analyses, uniform concentrations of the aforementioned elemental additives were maintained across all test samples. Table 1 provides the chemical composition of the used mixture. Deviations from the 100 % detection rate within Table 1 can be explained by elements with a lower concentration, measurement uncertainties, or oxygen (O), which could not be detected with the applied chemical analysis method (ICP-OES).

To calculate the graphite powder needed for a full reduction in the reactor, the cathode material's weight was factored by the molar ratio applicable to $LiCoO_2$. The oxygen moles were then ascertained by taking the oxygen's weight and multiplying it by its atomic weight. Subsequently, the mass of carbon required was figured out using carbon's atomic weight, assuming that it would entirely convert to carbon monoxide (CO) during the reaction. However, since carbon dioxide (CO_2) is most likely formed in the lower temperature range, the stoichiometric calculation for carbon is likely overestimated. According to these calculations, a full reduction of $LiCoO_2$ would need about 20 % carbon, which is in line with findings by Holzer et al., 2021 [27]. However, considering the addition of 2 % Al, which acts as a more potent reducing agent than C, is expected to lower the needed C percent. Thus, a carbon percentage of 17 % was chosen for the melting experiments.

2.2. Pyrometallurgical treatment

The pyrometallurgical processing of the feedstock was conducted in an inductively heated packed bed reactor, known as the InduMelt Reactor, a batch version of the InduRed reactor, where a schematic overview and comparison between batch and continuous reactor is given in Wiszniewski et al., 2023 [29]. The reactor's packed bed comprises graphite cubes, each with a side length of 25 mm, serving as the susceptor material. These cubes are positioned within a crucible crafted from refractory material, where the design and material of the crucible can change depending on the input material. The crucible's design, initially detailed in publications by Ponak [14], Holzer et al., 2021 [27], and Wiszniewski et al., 2024 [20], features a cylindrical upper section transitioning into a hemispherical base. A lid of refractory concrete, primarily comprising aluminum oxide (Al_2O_3), seals the top of the crucible, facilitating a regulated extraction of the gaseous products. A central hole punctuates this lid to accommodate an Al_2O_3 off-gas conduit. To curtail thermal dissipation, the crucible, the lid, and the off-gas pipe are covered by two or three layers of ceramic fiber blanket (mixture of Al_2O_3, SiO_2 and Cr_2O_3), resistant to a continuous temperature of 1500 °C.

The InduRed reactor is designed to enable efficient high-temperature processing through an optimized induction heating system. The apparatus consists of a copper induction coil, which generates the required

Table 1
Chemical composition of synthesized LCO black mass as a mass fraction in weight percent [%].

Substance	Li	Co	Fe	Cu	Al	C	O_2
%	5.6	47.7	3.0	3.0	2.0	17.0	22.7

magnetic field, in combination with a resonant circuit formed by a pair of capacitors. To maintain stable operating conditions, a cooling system ensures that both the coil and capacitors remain within a controlled temperature range of 16 °C–20 °C. A riser ring enhances energy transfer efficiency, ensuring optimal electromagnetic coupling around the middle segment of the reactor.

The melting zone, located at the reactor's uppermost section, is where black mass is continuously fed into the system within an argon stream. Upon contact with the heated graphite bed, the material instantaneously melts, forming a thin molten film or metal droplets on the graphite cubes' surface. The graphite cubes themselves serves a dual purpose: it maximizes surface area for subsequent reactions while also providing the desired heat directly at the surface of the cubes due to the skin-effect, resulting in an efficient energy transport. As the molten material progresses downward, it enters the reaction zone, where the primary carbothermic reduction reactions take place. This region is characterized by a highly reducing atmosphere, maintained through a low oxygen partial pressure and a CO-rich environment, achieved by the controlled addition of fine carbon powder, represented by the anode material. This atmosphere facilitates the gasification and volatilization of Li- and P-compounds, allowing their extraction via the gas phase, a key advantage over conventional pyrometallurgical recycling techniques, where Li is typically being oxidized and found in the slag phase. While the fine graphite powder within the input material is used for carbothermic reduction, the graphite bed itself mostly says unused due to its lower reactivity. The homogeneous radial temperature field and adjustable vertical temperature profile further enhance reaction kinetics, ensuring efficient Li and P recovery. Gaseous reaction products exit through an off-gas pipe, leading into an exhaust bell connected to a gas-washing bottle filled with distilled water, where Li and P deposition occurs. A waterjet pump at the end of the exhaust system provides the necessary negative pressure, ensuring effective gas flow and collection. In the discharge zone, located at the reactor's lower section, the final material properties can be fine-tuned via a third induction coil. This zone is particularly critical for maintaining the dynamic viscosity of the molten material, especially when overheating is required for atomization or slag spray applications. The production of a fine-grained output is advantageous for downstream hydrometallurgical or bio-hydrometallurgical leaching processes, where increased reactivity enhances efficiency. The precise temperature control in this zone enables continuous discharge, preventing process interruptions and ensuring operational stability.

Compared to conventional pyrometallurgical recycling, where heterogeneous temperature profiles often result in inefficient reaction conditions, the InduRed reactor offers superior process control due to its adjustable temperature zones. This flexibility allows for higher Li and P recovery rates, improving both the economic feasibility and the environmental sustainability of the process. Additionally, by utilizing renewable energy sources for heat generation, the InduRed reactor presents an additional benefit for improved sustainability within the sector of high-temperature recycling technologies.

The first new measurement tested within this paper, conducted a MgO crucible as used within Holzer et al., 2021, however with the addition of a layer of thin graphite, acting as diffusion barrier. This layer was applied by pouring 0.15 L of a liquefied carbon mixture (HC carbon - MECHANO-LUBE® 1VP1316) into the crucible and shifting it as long as the complete surface was covered with this carbon-enriched liquid. As the mixture's viscosity was high enough, a layer of about 0.5 mm was formed. Repeating this step two times, a layer of about 1 mm in total was formed. This layer was designed to be thin enough not to interact with the induced magnetic field but thick enough to form a protective layer. To avoid possible reaction between MgO and water to form $Mg(OH)_2$, the coated crucible was dried immediately after the coating process at 120 °C for 3 h. An illustration of the crucible is given in Fig. 1, while Table 2 provides an overview of the chemical composition of the MgO crucibles used in this paper.

Additionally, as shown in Wiszniewski et al., 2024 [20], a lid was used for improved gas extraction and was also covered with a layer of 1 mm of the liquefied carbon mixture.

The second concept revolves around a MgO crucible ingeniously filled with graphite cubes of varying sizes to provide areas of horizontal temperature gradients with lower temperatures closer to the crucible wall. The geometry of the graphite cubes is critical as it significantly influences the eddy currents generated and, therefore, how effectively the susceptor couples with the magnetic field. This behavior directly depends on the field's frequency and affects the resulting temperature, where a reduced susceptor size results in a lower temperature. A detailed explanation is given in chapter 2.3. To optimize this coupling, the crucible's design incorporates a cube size gradient, where half of the crucible is filled with cubes with a side length of 25 mm and the other half with graphite cubes with a side length of 10 mm. On a bigger scale with larger diameters, the smaller graphite cubes should be strategically placed close to the crucible walls in a circular and symmetrical way to

Table 2
Chemical composition of the MgO crucible in weight percent [%].

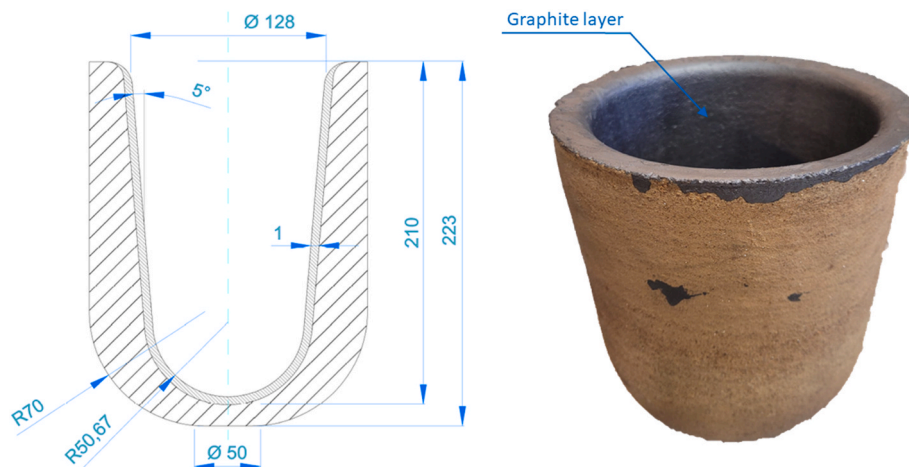| Compositions	Al_2O_3	SiO_2	CaO	MgO
%	0.1	0.5	1.1	97.5

Fig. 1. Design variation of a crucible used within the InduMelt reactor: MgO crucible with a layer of liquefied carbon mixture used as a diffusion barrier against Li. Dimensions are given in millimeter.

protect the whole crucible. As a result of the temperature gradient within the graphite cubes, a protective barrier can be formed by promoting the formation of a freeze lining, a solidified layer of the melt that adheres to the smaller cubes, acting as a corrosion shield and diffusion barrier. Towards the center of the crucible, the cubes are larger and selected for their ideal size to achieve optimal induction properties, thus, an ideal temperature level to accelerate the kinetics of desired reactions. This central arrangement allows for efficient heating of the melt while simultaneously contributing to the protective factor of the crucible wall. To emphasize and quantify the postulated influence of the cube size, half of the crucible was filled with the bigger cubes, while the other half was filled with cubes of reduced size. The crucible's temperature effectiveness is monitored using seven Type S thermocouples, which are insulated and positioned to measure the temperature gradient within the crucible, according to Fig. 2. The crucible had to be drilled using a column drilling machine to place the five thermocouples inside the reactor. Another two thermocouples, type S, were placed at the crucible's outer surface, approximately at the same height as the five inner thermocouples, to monitor the temperature of the outer surface of the crucible.

This trial aims to maintain a temperature profile high enough in the center for efficient melting but cooler towards the walls to ensure an increased melt viscosity, avoiding direct contact between refractory and melt. The formation of a freeze lining is with the small amount of input material not realizable. However, to provide comparability between each trial, the input mass was also limited to 0.4 kg, where all of the mass was placed on the top two layers of graphite cubes at the edge between smaller and bigger graphite cubes.

2.3. Mathematical model of induced temperature field within the InduRed reactor

Temperature plays a crucial role in both the thermodynamics and kinetics of the input material and in maintaining the integrity of the refractory. To explore these effects, a simulation was conducted using data from a calibration trial with homogenous graphite cube sizes.

Schönberg (2014) describes and explains the physical phenomena occurring within the susceptor material [15]. In essence, heat generation within the susceptor is driven by eddy currents that flow concentrically within its body. Based on the analytical solution for a cylindrical body, a direct analytical solution was also found for spherical bodies in Ref. [15]. Although slight differences may arise in practice, these solutions can be applied to cubic geometries. The mathematical quantification of this heat generation is derived from the power equation, which involves both current (I) and Ohm's resistance (R).

$$P = I^2 \cdot R \tag{1}$$

Utilizing the material equation C = E•κ (with C = current density, E = the electric field and κ = conductivity) and the specific electrical resistivity ρ, which is the reciprocal of the specific electrical conductivity κ, the power input into a cylinder per height is given by following equation:

$$\frac{P}{h} = \int_0^{r_0} 2 \cdot \pi \cdot r \cdot \kappa \cdot E^2 \cdot dr \tag{2}$$

By integration of the formula and a defined geometry considering the height of the cylinder, as well as the definition of k with $k = \frac{\sqrt{2}}{\delta}$ and with δ being the penetration depth within the susceptor defined as

$$\delta = \sqrt{\frac{1}{\pi \cdot f \cdot \mu \cdot \kappa}} \tag{3}$$

following formula for the induced heat input in the cylindrical body can be given as

$$P = \frac{\pi \cdot r_0 \cdot k \cdot h}{\kappa} \cdot H^2_{(r_0)} \cdot F_{(k \cdot r_0)} \tag{4}$$

As the volume decreases with smaller particles, the power induced at a constant field parameter including field strength and frequency, will be lower, resulting in a lower temperature increase. This relationship is further influenced by the magnetic permeability and electrical conductivity of the susceptor material, which also affect the depth of
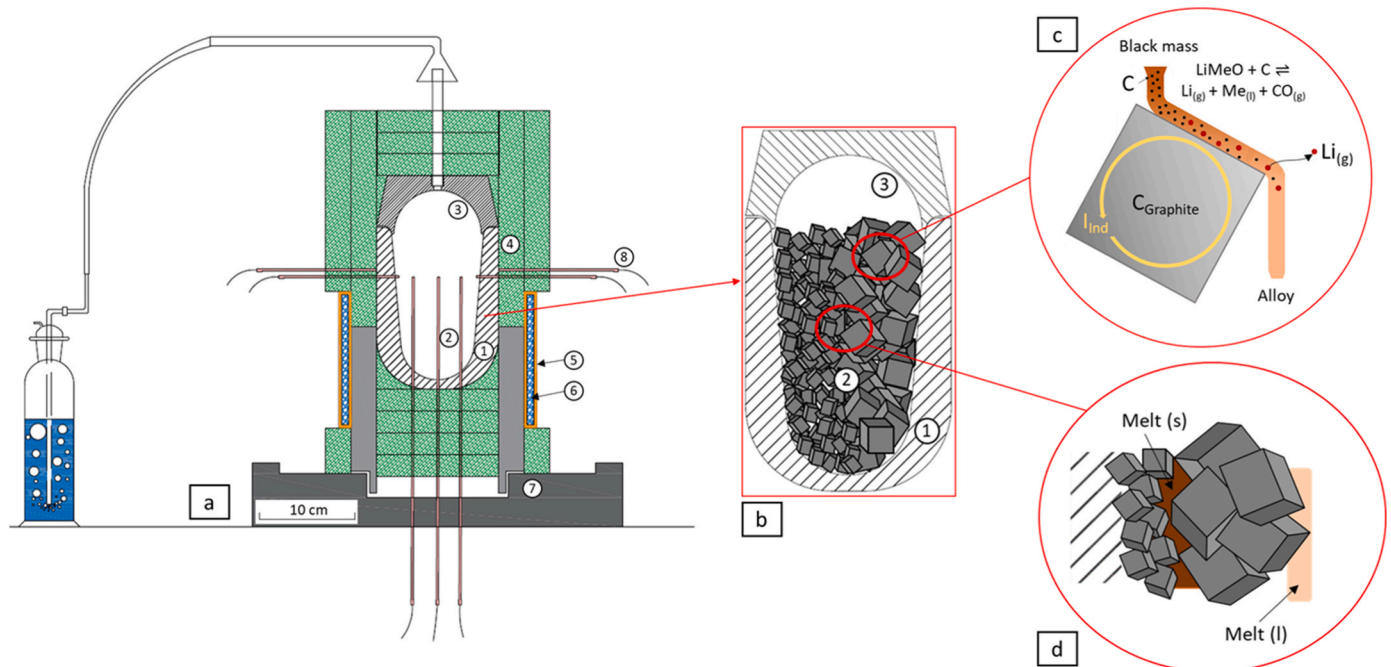

Fig. 2. a.) InduMelt setup with type S thermocouples to measure temperature gradients in a packed bed of varying susceptor material. ① Crucible (MgO), ② Area of susceptor material, ③ Area of gas atmosphere (turbulent), ④ Insulation, ⑤ Copper induction coil, ⑥ Water cooling (laminar), ⑦ Refractory concrete, ⑧ Thermocouple; b.) Crucible filled with varying sizes of graphite cubes; c.) Graphite crucible with reaction principle based on Ponak [14], d.) frozen melt layer, between varying graphite cubes based on temperature dependent dynamic viscosity.

penetration of the magnetic field and, consequently, the heating efficiency. The correlation between susceptor size, temperature, frequency and induced power is given within Fig. 3.

In Chapter 3.2.2, the temperature gradient, based on results from the calibration test with different graphite cube sizes, is given.

Temperature distribution, as a key factor for the pyrometallurgical carbo- and aluminothermic reduction within the system, has been estimated using numerical simulation in combination with experimental results that have been used to define necessary boundary conditions. Raynolds Averaged Navier Stokes equations for the case are formulated and solved in the OpenFOAM Multi-Region framework as follows.

$$\frac{\partial \rho}{\partial t} + \vec{\nabla} \cdot (\rho \overline{u}) = 0 \tag{5}$$

$$\frac{\partial \rho \overline{u}}{\partial t} + \vec{\nabla} \cdot (\rho \overline{u} \, \overline{u}) = \vec{\nabla} \cdot \overline{\tau} - \vec{\nabla} \, \overline{p} + \rho \vec{g} - \vec{\nabla} \cdot (\rho \overline{u'u'}) \tag{6}$$

$$\frac{\partial \left[\rho \left(e + \frac{\overline{u}^2}{2} \right) \right]}{\partial t} + \vec{\nabla} \cdot \left[\rho \overline{u} \left(e + \frac{\overline{u}^2}{2} \right) \right] = \overline{u} \cdot [\vec{\nabla} \cdot \overline{\tau} + \vec{\nabla} \, \overline{p}] + \vec{\nabla} \cdot q + \dot{S}_S \tag{7}$$

with e as inner energy, ρ is the density, u is the velocity vector, p stands for pressure, τ is stress tensor, $\vec{g}$ gravitational acceleration, and t stands for time.

Equation (5) represents the continuity equation without additional mass source term in the system. Equation (6) describes the change in momentum (impulse) within the system due to external forces. The first term on the left-hand side accounts for stretching or compression, with volumetric dilation being relevant only for the incompressible flows. The subsequent terms represent the pressure gradient and gravitational force, while the final term corresponds to the Reynolds Stress Tensor, which models turbulence phenomena using the k-epsilon model. For the water region, used as a cooling medium for the coils, laminar flow was assumed due to the low Reynolds number within the 3-mm-wide flow gap.

The terms on the right-hand side of Equation (7) account for the contributions of surface forces, pressure gradient forces, and conductive energy transport. The final source term represents the source term for the radiative heat transfer.

In the pyrometallurgical reactor, where high temperatures prevail, radiation becomes a key factor because heat transfer scales with the
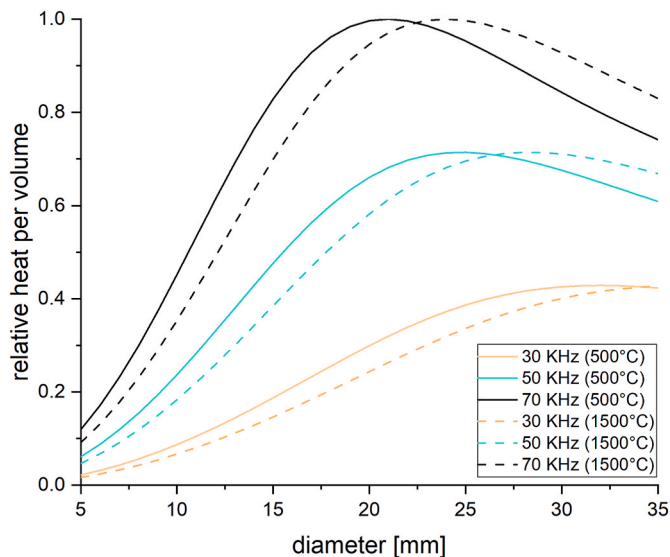

Fig. 3. Calculated relative induced heat per volume in a packed bed of spherical particles depending on particle size for different frequencies and temperatures.

fourth power of the temperature difference. Unlike radiation, convection and conduction exhibit nearly linear dependencies. When radiation contribution is significant, electromagnetic waves may undergo emission, absorption, or scattering by the medium. The propagation of thermal radiation through the participating medium between boundary walls with the packed bed is modeled using the radiative transfer equation with the discrete ordinate method, which is formulated for the direction s of the solid angle as follows:

$$\frac{\partial I}{\partial s} = -(a + \sigma_s) \cdot I + e \frac{\sigma T^4}{\pi} \tag{8}$$

I stands for the radiation intensity, a is the absorption, e is the emission and σ_s is the scattering coefficient, with σ as the Stefan-Boltzmann constant. The term that describes scattering phenomena can be neglected for the implementation case, as well as the participation of the gaseous phase due to negligibly low concentration of H_2O and CO_2, i.e., absorption and emission coefficients in the fluid phase are set to zero.

In the solid regions, energy transport is solved for each solid region separately using the following formulation for the enthalpy transport equation:

$$\frac{\partial(\rho h)}{\partial t} = \nabla \cdot [\alpha(T) \nabla h] + S_i, \alpha(T) = \frac{\lambda(T)}{cp(T)} \tag{9}$$

λ is the thermal conductivity and cp stands for the specific heat capacity of the solid material.

Thermal conductivity and specific heat capacity as the function of the temperature are approximated by the polynomial functions based on the datasheets for the specific material:

$$\lambda(T) = c_1 T^2 + c_2 T + c_3 \tag{10}$$

$$cp(T) = p_1 T^3 + p_2 T^2 + p_3 T + p_4 \tag{11}$$

The energy transport at the interface between fluid and solid regions is defined with the following condition:

$$\lambda_f \frac{dT_1}{dn} + Q_{rad,f} = -\lambda_2 \frac{dT_2}{dn} - Q_{rad,s} \tag{12}$$

T is the temperature, Q_{rad} radiative heat, n is the normal direction of the surface and indices f and s represent fluid and solid sides, respectively.

The temperature profile measured on the packed bad surface and corrected for the radiative influence as described in Legenstein 2021 [30], is a function of distance z along the rotation axis from the bottom of the crucible and radial distance, given by the following relation:

$$T_i(z, x, y) = p_1 \cdot z + p_2 - \left[p_3(z) \cdot \sqrt{x^2 + y^2} + p_4(z) \right] \tag{13}$$

Based on equations (5)–(13), Fig. 4 provides an overview of the temperature distribution within the crucible and the susceptor material, with the temperature-colored streamlines in the continuous gaseous phase.

2.4. Analytical methods

A set of different analysis methods was applied to investigate whether the two different designs of the crucible were beneficial regarding Li diffusion and to see if the different designs provide properties to protect against corrosion. To gather an overview of the potential corrosion of the crucible from the InduMelt trials, microscopic X-ray fluorescence analysis (µXRF) with a Bruker M4 Tornado was used. As µXRF analyses cannot detect elements with a periodic number smaller than 11 (sodium), selected crucibles and metal phases were additionally analyzed regarding Li via X-ray diffraction (XRD) measurements. For this purpose, a Bruker D8 advance in Bragg-Brentano geometry with Cu Kα radiation (λ = 0.15418 nm) at 25 mA and 40 kV was used. Diffraction patterns were collected in the 2θ range from 5° to 70° with a step size of
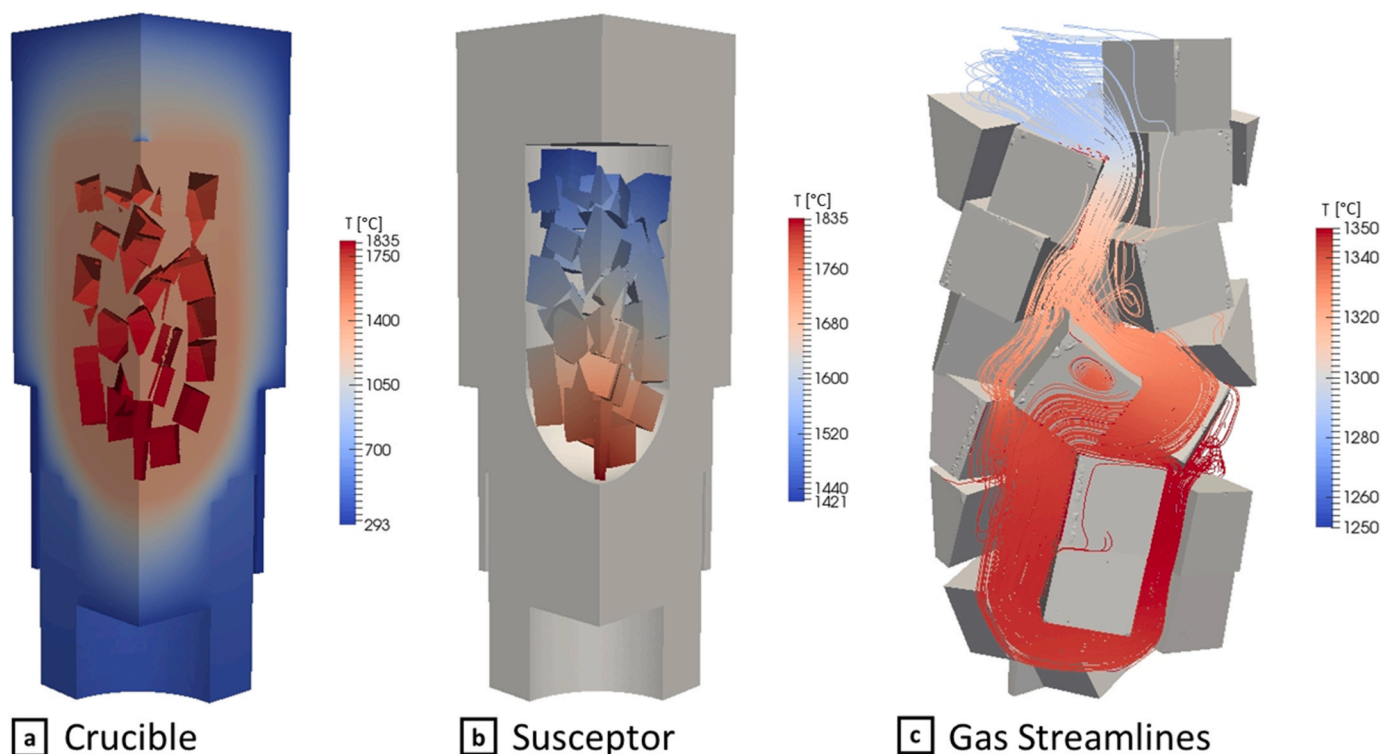
Fig. 4. Mathematical simulation of different elements of the reactor. a.) crucible, b.) susceptor material, and c.) gas flow temperature distribution in a randomized packed bed.

0.01° and 1 s acquisition time per step and analyzed via the SIeve + software with PDF-4+ 2022 database (ICDD, USA). Additionally, the crucible was investigated using scanning electron microscopy (SEM) and energy-dispersive X-ray spectroscopy (EDX) to investigate fractures within the material or elemental compositions at the micrometer scale. Therefore, a ZEISS EVO MA 15 with attached EDX from Oxford instruments (Ultimax 65) was used.

The investigation of a potential formation of a freeze lining for refractory protection was based on temperature-dependent dynamic viscosity. Viscosity measurements have been conducted using a high-temperature rotary rheometer from Anton Paar (FRS 1800, DSR 502) with a C-ETD 1800 Carbolite Controller for temperature control and a VT2 as a fluid circulator. This device is a suitable measurement method for multicomponent systems with inclusions, as they can occur in real processes. This technique allows for accurate determination of the viscosity of complex systems under various shear conditions.

Samples of the solid fractions after the carbothermic reduction and the purifying water after the off-gas route were investigated via ICP-OES according to ÖNORM EN ISO 11885:200911. This was done to investigate the mass fraction of Li in the different products and compare the results to qualify the benefits of the diffusion layer.

3. Results

Previous results using the InduMelt plant for carbothermal reduction of LIB materials have shown that the most common refractory materials, such as MgO or Al_2O_3, suffer from severe diffusion or corrosion problems [18,19]. In a previous study, crucibles made out of SiC showed superior corrosion resistance, minimal Li or other volatile elements diffusion, and high thermal shock resistance. Although SiC proved to be a very promising solution for the aggressive conditions occurring during pyrometallurgical recycling of LIB material, several problems must be tackled. Especially, the diffusion of Li and sulfur (S) could lead to a potential mechanical weakening over time in a continuous approach [20]. One solution for 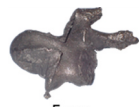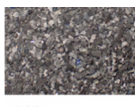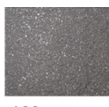Li diffusion is the application of a thin layer of very dense material, such as carbon, which is very insensitive to Li diffusion. As further research regarding SiC has to be done, MgO was chosen as a refractory material. As MgO is highly susceptible to Li diffusion, the use of MgO could also better show the effectiveness of the different approaches within this study, compared to refractory materials where Li diffusion is limited, such as SiC or Cr_2O_3 [20].

3.1. Elemental distribution and Li extraction

For reference, one crucible without any modification was used, further stated as LCO_Ref. Results from the crucible with the C layer are further linked to LCO_C, and results from the crucible with varying graphite cube sizes are linked to LCO_Ss, where Ss stays for the different sizes of the susceptor material. For all trials, the lid and insulation were removed once the crucible was cooled to room temperature after approximately 48 h. Except for LCO_Ss, the graphite cubes and the different solid product phases consisting of alloy, slag, and powder phases were removed and classified using magnetic separation and sieving up to a grain size of 250 μm. The LCO_Ss crucible was filled with an epoxy resin to stabilize the inner occurrence, making removing the solid products impossible after the trial. As a result, the solid product phases' mass balances and chemical analyses have only been conducted for the crucible LCO_Ref and LCO_C, as shown in Table 3. However, a qualitative analysis for the gas phase based on the corresponding solution from the gas scrubber was performed for all three trials, as shown in Table 3.

Table 3 presents a comparative analysis of the LCO_Ref and LCO_C trial, focusing on the mass distribution and chemical composition of various fractions resulting from each trial. The total mass of the products indicates a higher yield for the LCO_C trial, with 227.6 g compared to 224.1 g for the LCO_Ref trial. This suggests that the modification using a graphite-coated crucible may have enhanced the recovery efficiency by limiting contact with the refractory and avoiding infiltration. In Fig. 5, a Sankey diagram illustrates the element's preferred transformation pathways according to their thermodynamic stability. The diagram

Table 3

Overview of mass fractions in gram and elemental composition in % of the different phases after treatment within the InduMelt reactor for the trials LCO_Ref and LCO_C using 400 g of input mass according to Table 1.

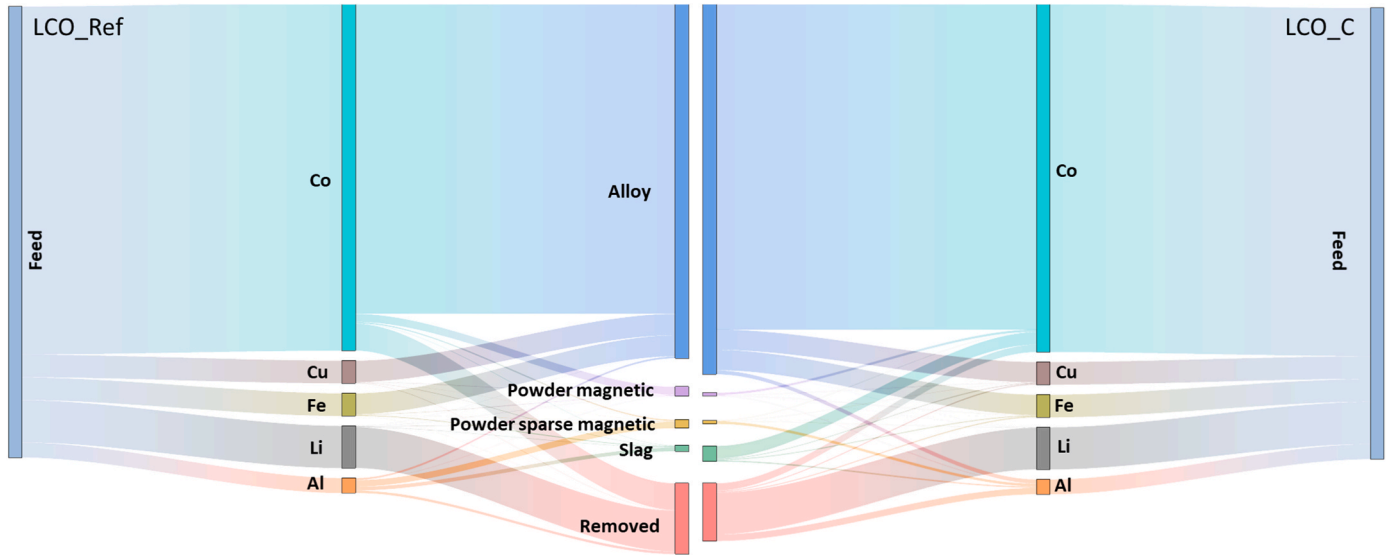|		Alloy	Slag	Powder magnetic	Powder sparse magnetic
		5 cm	2 cm	100 µm	100 µm
Mass/g	LCO_Ref	206.06	6.78	5.26	5.97
	LCO_C	214.25	8.68	1.87	2.79
Li/%	LCO_Ref	0.04	3.55	2.58	5.04
	LCO_C	0.03	0.16	2.91	4.26
Co/%	LCO_Ref	79.38	46.40	80.40	12.76
	LCO_C	79.83	76.33	66.63	6.61
Cu/%	LCO_Ref	5.36	7.05	5.83	1.37
	LCO_C	5.01	5.78	8.43	0.84
Fe/%	LCO_Ref	5.47	3.45	4.10	0.93
	LCO_C	5.01	4.93	8.37	3.77
Al/%	LCO_Ref	0.51	29.74	2.39	57.09
	LCO_C	0.99	8.39	9.17	50.75

Fig. 5. Sankey diagram of the input and output streams after treatment within the InduMelt reactor for the trials LCO_Ref and LCO_C (for better visualization and comparison, LCO_C is mirrored).

highlights how certain elements migrate or react to form more stable compounds under given conditions. For instance, lithium prefers to integrate into oxide phases such as the slag phase, while cobalt shows a strong affinity for remaining within metallic or alloyed states. This thermodynamic tendency is crucial for understanding and optimizing recovery and separation processes in metallurgical applications. The majority of the recovered mass in both trials is found in the alloy fraction, with 206.06 g within LCO_Ref and 214.25 g within LCO_C. This dominance of the alloy fraction highlights its significance in the overall mass balance, a crucial fact considering further refining steps to close the material cycle for battery production. Also, the slag fraction is significantly higher, with 8.68 g within LCO_C compared to the LCO_Ref trial with 6.78 g, indicating a different behavior in the waste or byproduct formation and potential infiltration of the crucible. The magnetic and sparse magnetic powder fractions also exhibit notable differences between the trials. Within LCO_Ref, these fractions collectively amount to 11.23 g, whereas for LCO_C, they sum up to 4.66 g. This reduction in the second trial might reflect a more efficient separation or a different interaction with the graphite layer, possibly influencing the material's magnetic properties and segregation behavior.

Chemical composition analysis reveals variations in the distribution of key elements like lithium, cobalt, copper, iron, and aluminum across different fractions. For instance, the alloy fraction within LCO_C contains a higher cobalt content, suggesting a more effective retention or recovery process. While the recovery rate for cobalt within LCO_C was as high as 97.8 %, the recovery rate for LCO_Ref was lower, with only 92.3 % considering only the alloy fraction. In contrast, lithium is predominantly found in the removed part, with 98.8 % for LCO_C and 96.7 % for LCO_Ref. These results collectively suggest that using a graphite-coated crucible increased the total mass of recovered products and influenced the distribution and concentration of various elements within different fractions. The data also highlights the importance of optimizing experimental conditions to achieve desired recovery rates and purity levels in metallurgical and recycling operations. These results show that layers of dense materials such as C can significantly influence the overall effectiveness of pyrometallurgical recycling of LIBs. Next to carbon as a layer, future research could focus on other coatings such as boron nitride (BN), titanium carbide (TiC), or silicon nitride (Si_3N_4). Also, carbon could be used as crucible material. However, to avoid magnetic coupling of the crucible and becoming an unintended heat sink, the crucible has to be

engineered with a narrow slit filled with an electric isolating ceramic. This has to be done to enhance its functionality within an inductive heating environment. By integrating this MgO gap, the crucible is engineered to remain largely unaffected by the magnetic field, allowing the graphite cubes within the crucible to be heated. In contrast, the crucible itself stays at a lower temperature. As one of the primary goals of this experiment was to identify the impact of different crucible designs on the extraction rate of Li, the off-gas scrubber solution and the precipitates from the solution were analyzed regarding their Li content. Results are given in Table 4.

The results of Table 4 indicate a much higher Li extraction using the LCO_C crucible with the protective carbon layer. The concentration of Li in the scrubber solution is higher, as well as the amount of precipitate and the Li concentration within it. As shown in Wiszniewski et al., 2023 [29], most of the precipitates tend to be lithium carbonate (Li$_2$CO$_3$), with some impurities consisting of the remaining elements of the input material, which can be carried along in the exhaust stream and separated in the scrubber solution.

3.2. Refractory corrosion and diffusion behavior

This chapter provides the microstructure of the different crucibles with and without modifications using μXRF, XRD, and SEM-EDX analyses. Fig. 6 shows the XRD spectrum of the unused MgO crucible, with the most dominant phases being Periclase (MgO), Monticellite (CaMgSiO$_4$ -CMS), and Forsterite (Mg$_2$SiO$_4$ – M2S).

Furthermore, the viscosity of the metal product obtained from the InduMelt trial LCO_Ref is measured in a temperature range from 1250 °C to 1600 °C. In combination with the temperature calibration of the InduMelt crucible, this test series investigates whether a solidified layer close to the refractory could potentially form.

3.2.1. Microstructure analysis

To analyze whether the fraction "Removed" can be attributed to the gas phase, to the crucible, or to a combination of both, the crucible is investigated qualitatively via μXRF, XRD, and SEM-EDX. μXRF analyses can provide an overview of corrosion, infiltration, and diffusion of the whole crucible. Fig. 7 shows the elemental mapping of the cross-section from each trial for different elements. As can be seen, the intensities for Cu and Fe vary enormously between each trial. While the intensity is high for LCO_Ref, the intensity for LCO_C is lower and for LCO_Ss there is almost no sign of Fe and Cu anymore, indicating the effectiveness of the different designs. Additionally, it appears that there is a reaction between the crucible on the outer side and the ceramic fiber mat, used as thermal insulation, showing high peaks for silicium (Si) and calcium (Ca). Since the insulation material consists mostly of SiO$_2$, Al$_2$O$_3$, Cr$_2$O$_3$, and CaO, also typical components of industrially used slag formers, this might be a concerning issue for the use of a continuous approach, where slag formers may be needed to improve the fluidity of the melt. However, the usage of slag formers and their implications on the refractory material was not further investigated within this study but will be investigated in future research.

The μXRF images for LCO_C also showed some signatures of higher intensity of iron and copper, which are likely due to surface contamination from the cutting process rather than infiltration during the high-temperature tests. Looking at the Co signature within Fig. 7, no signs of

Table 4
Chemical analysis of the off-gas scrubber solution and corresponding precipitates for the three different crucible designs.

	Li in off-gas scrubber solution in mg/l	Precipitate in g	Li mass fraction in percent [%]
LCO_Ref	230	0.07	2.87
LCO_C	310	0.26	9.33
LCO_Ss	192	0.09	7.41

corrosion and infiltration were seen at any trial, a remarkable result comparing the findings within Wiszniewski et al., 2024 [20], where Co showed to be the most aggressive component within LIBs. Considering the elemental mapping within LCO_Ss, it is macroscopically seen that there was no contact between the melt and the refractory, explaining why no infiltration or corrosion was possible. This demonstrates the effectiveness of using smaller susceptor material closer to the crucible wall as a mechanical and thermal shield. However, Li could not be investigated via μXRF, so XRD and SEM-EDX were used in the next step. Additionally, small cracks were detected within LCO_Ref and LCO_C along the inner and outer surface, where SEM-EDX analyses provide a proper analysis method to define possibilities for the origin of this behavior. The interaction between Li and the refractory can be qualified by XRD analyses.

Similar phases have been detected in all three crucibles, only differentiating within their peak intensities. Fig. 8 shows the XRD spectra, including SEM images with corresponding EDX analyses for the crucible LCO_Ref sample. Next to similar phases found in all trials, repeatable sampling of an inner, middle, and outer area is hardly possible, which is why comparing XRD and SEM analyses between each trial is not favorable and has to be explored in more detail in future studies. However, the crucible shows discolorations not only on the outside but also in the cross-section of the wall, which reveals a clearly recognizable color zoning. Inside, each crucible is greyish due to contact with either carbon of the input material, from the graphite cubes, or due to the CO atmosphere. This greyish area is similar within all three trials and was identified as a carbon-rich phase. Considering the LCO_Ss crucible, the side in contact with the bigger graphite cubes, however, shows a zone where this greyish area impacts almost the whole cross-section up to the outer wall. In contrast, the side in contact with the smaller graphite cubes shows a much smaller blackened area (visible in Fig. 10), most likely due to decreased temperatures and therefore limited infiltration and diffusion. In all crucibles, expect LCO_Ss, this area is followed by a pinkish zone, of which the thickness varies across the cross-section and is attributed to contamination, either by Li or due to other elemental diffusion. For LCO_Ref this zone is thinner at the top and extends almost to the outside at the bottom. For the most part the discoloration reaches up to the middle or two-thirds of the wall thickness from the inside. For LCO_C and for LCO_Ss in contact with the smaller graphite cubes, this area was much lower, highlighting the ability to protect the crucible from diffusion or infiltration. The outside of the crucible is yellowish, corresponding to the color of an unused bonded magnesia product. The outermost layer shows again discoloration in greenish from the previously applied insulation. These phenomena are highlighted in Fig. 8, where crucible fractures of the middle part of each test were taken as testimonial for visual comparison.

Looking at the microstructure of LCO_Ref (Fig. 9) the crucible exhibits a porous structure on the outside and in the outer third. Among the large periclase grains (MgO), there is light-appearing monticellite (CaMgSiO$_4$, CMS) and darker forsterite (Mg$_2$SiO$_4$, M$_2$S). These phases were confirmed through XRD analysis. The structure is denser in direct contact with the surrounding ceramic fiber mat, and the periclase grains are rounded. Additionally, spinel (MgAl$_2$O$_4$, MA) has formed, embedded in a matrix of forsterite. The middle section is open-pored like the lower section. However, the grain edges are more eroded. Towards the inside of the crucible, forsterite is replaced by Li$_2$MgSiO$_4$ (LiMS) due to the diffusion of lithium into the crucible. The penetration of lithium likely resulted in lower eutectic points. In the gaps, needle-like crystals of Li$_2$MgSiO$_4$ can now be found within light-appearing Li$_2$CaSiO$_4$ (LiCS). Additionally, neither monticellite nor forsterite is detectable in the middle pinkish area in the XRD spectrum. The structure is also porous at the inner surface. However, the corrosion of individual grains is most advanced here. Metallic droplets of Cu and Fe can be seen directly at the surface. Bright spots can be observed in the periclase grains, which are likely made of Fe, although their size prevented analysis. In this direct contact zone, Li$_{2.4}$Mg$_{0.8}$SiO$_4$ is present in the crevices. With increasing
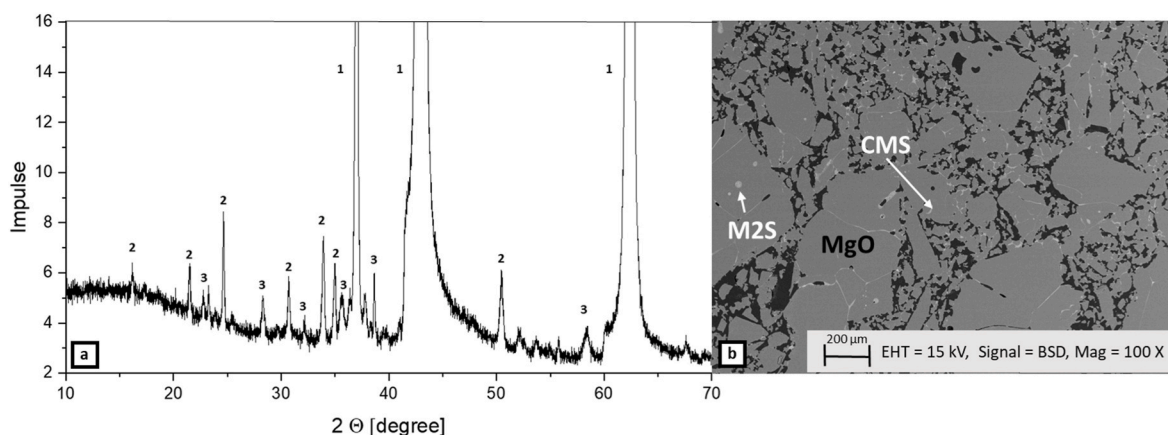
Fig. 6. XRD spectrum of an unused MgO crucible with three main phases: Periclase, Monticellite and Forsterit

distance from the inner surface, the crevice phases consist of Li_2MgSiO_4, within which fine bands of Li_2CaSiO_4 are present. Additionally, the XRD shows graphite from contact with the susceptor material, which can also be responsible for the macroscopic gray coloration in this area. As the periclase spectra were so dominant, with intensities of up to 1600 cps, the spectra for the other phases disappeared in the background noise. The scale was limited to a range from $+2$ to $+16$ cps to avoid these phenomena.

Considering thermodynamic calculations using FactSage™, in the binary system of Li_2MgSiO_4 - MgO, a melt tends to be stable alongside MgO and Li_2MgSiO_4 across the entire compositional range from 1363 °C onwards. From 1554 °C onwards, the only solid phase in the melt is MgO. Contrary, in the Li_2CaSiO_4 - MgO binary system a first melt appears already at 986 °C, with only MgO present in the melt from 1100.76 °C onwards. In the coexistence of Li_2MgSiO_4 and Li_2CaSiO_4, FactSage predicts the formation of a melt starting at 986 °C, existing across the entire compositional range. The coexistence of these two phases was already confirmed by XRD and SEM-EDX analysis within Fig. 9d, showing that this low melting phase can lead to potential wear of the crucible. The according binary phase diagrams can be seen in Fig. 10. For this calculation FactSage 8.3 with the databases FactPS and FToxide were used.

3.2.2. Temperature dependent viscosity as an approach for refractory protection

For further protection of the refractory lining against corrosion and diffusion, forming a zone utilizing lower viscosities could be an interesting option, especially considering a continuously operated reactor where the refractory lining eventually degrades. Considering a top-down operated packed bed reactor such as the InduRed reactor, also abrasion could potentially stress the refractory lining, leading to an even increased wear. A solution to these effects could be found in the use of freeze linings, layers of solidified bath material forming between the furnace shell or refractory and the liquid bath. In the case of the InduRed reactor concept, a freeze lining could be applied by two options. A proven way of providing a frozen metal/slag layer upon the castable refractory is by outer cooling via a cooling medium such as oils, water, or air [31,32]. Especially oils could be interesting in leveraging higher boiling points than water and electrical insulating properties, considering surrounding electrical equipment such as the induction coils. Another solution for implementing a freeze lining and thus protecting the crucible could be the use of varying sizes of susceptor materials, directly influencing the induced power and, therefore, temperature. By reducing the size of the susceptor, the temperature decrease when the frequency remains constant, which is ideally set for larger graphite cubes. The physics and normalized temperature curves are already described in materials and methods and shown within Fig. 3. The

temperature has a direct influence on the viscosity of the melt, which is a critical factor in the wear of refractory linings and the potential formation of a freeze lining. Viscosity influences the lubrication provided to the mold, the erosion rate of submerged entry nozzles, and the likelihood of slag entrapment. High-viscosity melts can reduce wear by minimizing slag flow, while low-viscosity melts can increase wear due to their greater fluidity and higher impact on the refractory walls. Typically, the temperature at which melts start to flow is closely related to their viscosity, whereas for slags to flow, the viscosity should ideally be between 2.5 Pa s and 25 Pa s [33]. Below this range, excessive wear can occur,due to increased fluidity, while slag blockages can form above it. Next to the temperature, the dynamic viscosity is also influenced by the chemical composition of the slag. Network formers like SiO_2 and Al_2O_3 increase the viscosity, while network breakers such as CaO, MgO, MnO, and FeO, as well as fluxes like Na_2O, K_2O, and Li_2O, decrease it [34–36]. Kinetic studies of carbothermal reduction of $LiCoO_2$ show that the formation of Li_2O is likely to happen at lower temperatures, therefore decreasing the viscosity of the melt [37]. However, the InduRed reactor, with its unique conditions, is likely to avoid the formation of high amounts of Li_2O in the melt by gasification of Li and extraction via an off-gas pipe. This thesis is supported by the results shown in Table 4, where high concentrations of Li were found and is a further advantage considering refractory protection.

However, these compositions need to be carefully controlled to maintain optimal viscosity, protect the refractory lining, and guarantee ideal processability within the reactor. Developing models tailored to the input materials are crucial in predicting the behavior of slags and preventing wear and damage to refractory materials. In Fig. 11b the crucible for the viscosity test and the corresponding viscosity are shown. As can be seen, the inclusions within the melt are the reason for the slag-like viscosity of the melt. These inclusions where identified as C, mostly likely resulting from an overstoichiometric supply of C within the input material. This highlights the importance of a precise definition of the ideal amount of carbon content within the input material, where the only possibility lies in optimal designed pre-treatment processes. Although the viscosities of pure alloys are normally lower between 2 mPa · s to 9 mPa · s [38,39], the viscosity measured within this test ideally represents the conditions within the InduRed reactor. As seen, the viscosity drastically increases between the temperature range of 1290 °C and 1250 °C. This ideally corresponds with Fig. 11c, where it is shown that the temperature close to the wall is already slightly below 1250 °C. Therefore, the formation of a solidified layer can be expected using this design variant within a continuously operated reactor.

However, the formation of a freeze lining within the described setup could not be achieved due to several limitations inherent in the experimental conditions. The limited quantity of input material and the batch operation mode, which restricted continuous flow within the spaces
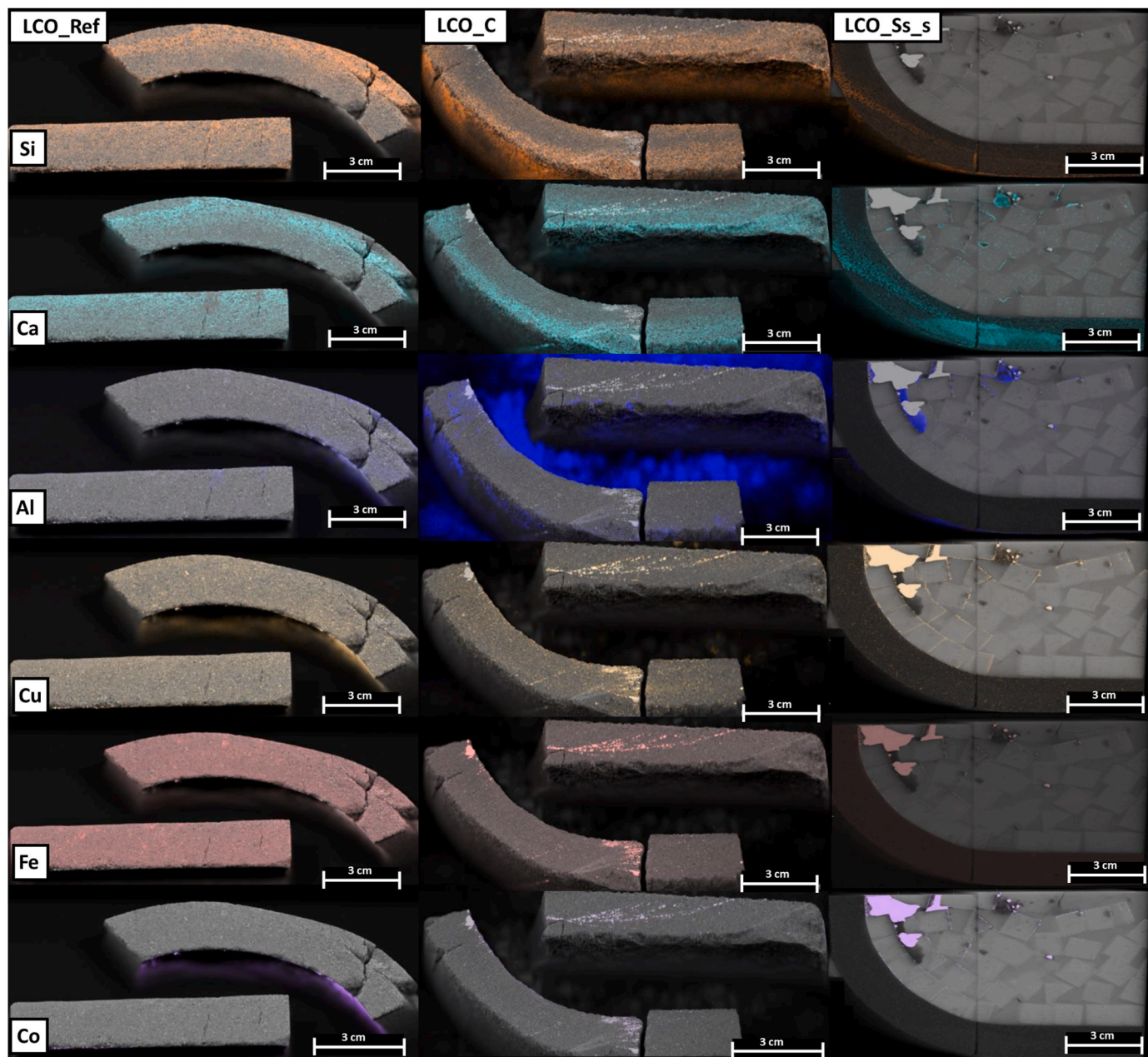
Fig. 7. μXRF analysis of different crucible designs after InduMelt trials including elemental mapping for Si, Ca, Al, Cu, Fe and Co.

between the smaller graphite cubes, significantly hindered the formation of a stable freeze lining. However, some promising observations were made at the bottom of the reactor. It was noted that an alloy managed to flow between the spaces, albeit only to a certain depth. This partial penetration indicates the potential viability of the concept, even if full formation was not achieved under the current conditions. Moreover, it was observed that no metal came into direct contact with the refractory lining, preventing any corrosion or infiltration. This outcome suggests that the design effectively protected the refractory material in specific areas even without a fully developed freeze lining. A macroscopic examination revealed significant diffusion on the refractory side where the temperature was higher, particularly on the side with the bigger graphite cubes. In contrast, the side with smaller graphite cubes showed minimal diffusion signs (Figs. 11a and 8c). This difference underscores the importance of thermal management and material flow in protecting the refractory lining.

In addition, it was found that the alloy tended to form small droplets rather than a thin, continuous layer of melt. This droplet formation could influence the gasification of volatile elements, an aspect that warrants further investigation. Understanding this behavior is crucial for optimizing reactor performance, particularly in processes where gas-phase reactions are significant.

4. Conclusion and outlook

This study investigated two distinct crucible modifications for their effectiveness in preventing lithium diffusion and corrosion within the InduRed reactor, which is used for the carbothermal reduction of $LiCoO_2$ synthesized black mass. One design involved coating the crucible wall with carbon to mitigate lithium diffusion, while the other used susceptor materials with varying geometries to create a temperature gradient aimed at reducing corrosion. A standard, unmodified MgO crucible served as a control.

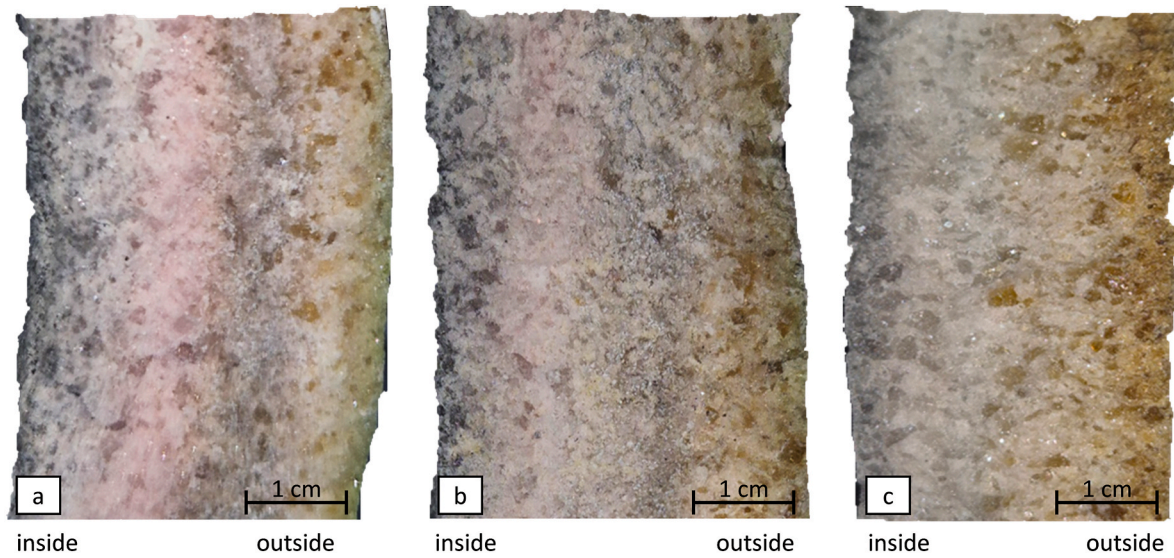Findings revealed lithium diffusion across all three crucible variants,

Fig. 8. Diffusion phenomena visualized by different coloring zones of used magnesia crucibles after pyrometallurgical treatment in the InduMelt: a.) LCO_Ref, b.) LCO_C and c.) LCO_Ss_s
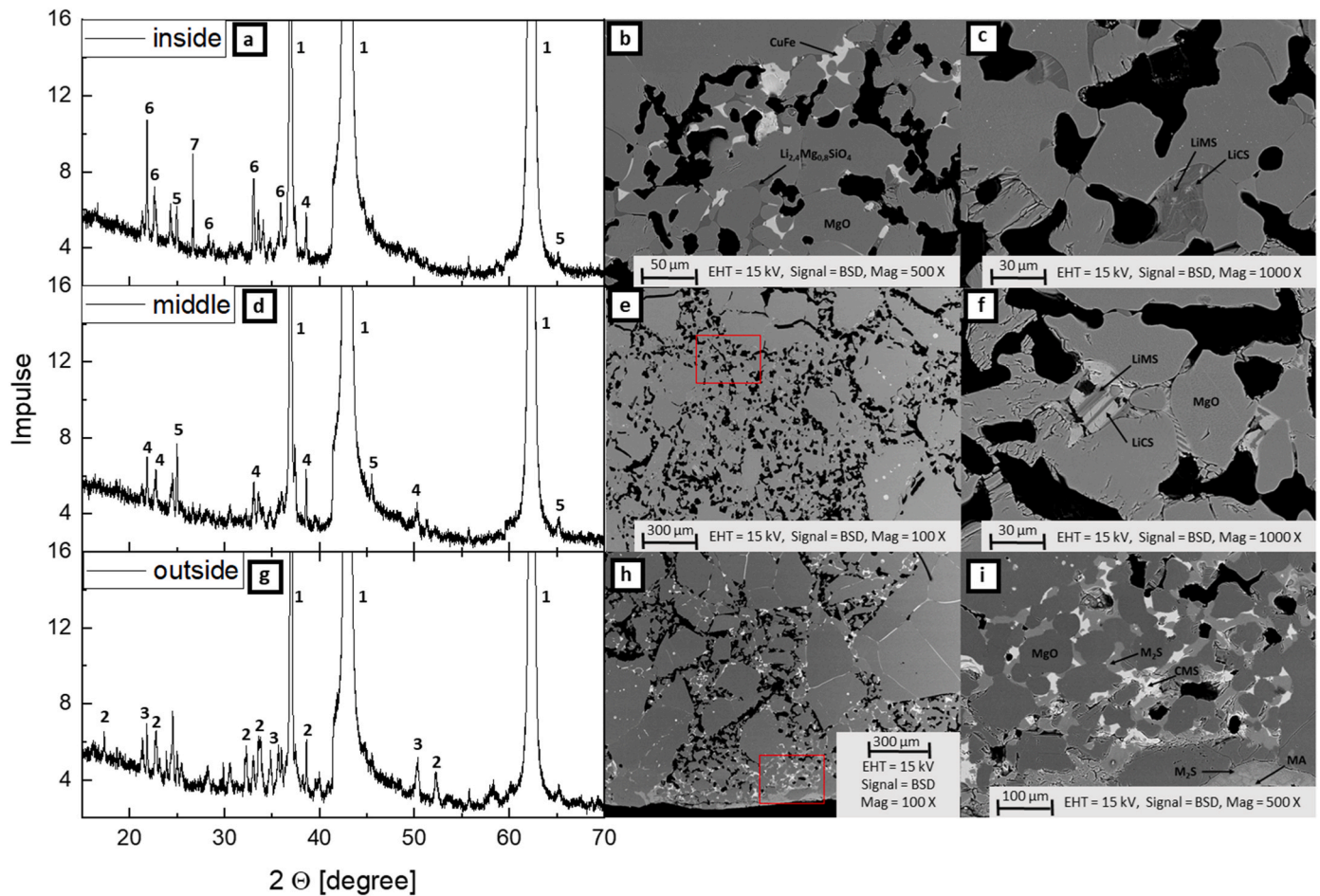

Fig. 9. XRD spectra of the LCO_Ref crucible from a.) the inner surface zone (inside), d.) from a zone in the middle of the crucible (middle), and g.) from a zone at the outer layer of the crucible (outside) with corresponding SEM-EDX analyses. Phases within the XRD spectra can be attributed as following: 1: MgO, 2: Mg_2SiO_4, 3: $CaMgSiO_4$, 4: Li_2MgSiO_4, 5: Li_2CaSiO_4, 6: $Li_{2.4}Mg_{0.8}SiO_4$, 7: C. SEM images: b&c.) inside, e&f.) middle pinkish layer, h.) outer layer at the bottom of the crucible with CuFe inclusions, i.) outer layer at the top of the crucible with LMS and LCS phases.
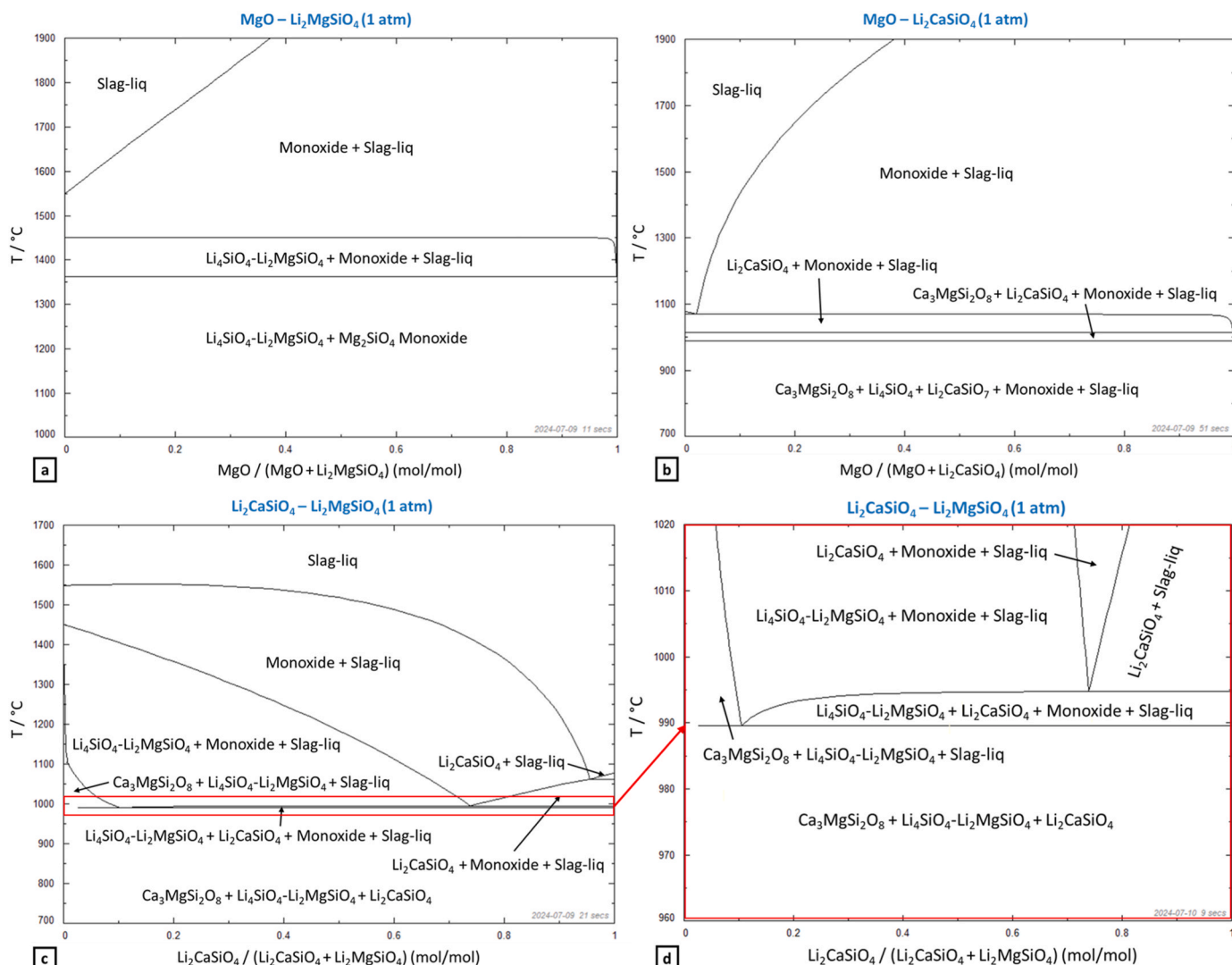
Fig. 10. Binary phase diagrams calculated using FactSage 8.3 for the systems a.) MgO - Li_2MgSiO_4, b.) MgO - Li_2CaSiO_4 and c.) Li_2MgSiO_4 - Li_2CaSiO_4 (large temperature window), d.) Li_2MgSiO_4 - Li_2CaSiO_4 (small temperature window).

with the unmodified crucible exhibiting the most prominent XRD spectra. Lithium from the raw material permeated the crucible material, triggering a series of transformations. Initially, this diffusion caused the bonding phases monticellite ($CaMgSiO_4$) and forsterite (Mg_2SiO_4) to convert into Li_2MgSiO_4 and Li_2MgCaO_4. FactSage Thermodynamic calculations using Factsage™ 8.3 indicated that these phases' coexistence resulted in melt formation at temperatures as low as 986 °C. Examination of the crucible interior using SEM-EDX showed that lithium diffusion and subsequent melt formation disrupted the ceramic bonding between periclase grains, leading to heightened corrosion. Consequently, this type of MgO crucible proved unsuitable for LIB recycling within the InduRed reactor without further modification.

Regarding element recovery rates, the graphite-coated crucible demonstrated impressive performance, achieving transfer coefficients above 90 % for all elements and up to 99 % for lithium. Analyzing the washing solution from the gas scrubber, including the precipitate, a tenfold of Li was found compared to the reference crucible. However, as most of the Li could not be found after each trial, it remains unclear whether the lithium was fully extracted via the gas stream or predominantly diffused into the crucible.

Considering the freeze-lining concept, the image and analysis results of the cross-section of the crucible with varying susceptor sizes indicated an advantage. Almost all the crucibles' cross-sections remained unaffected after high-temperature treatment. µXRF analyses also proved that no contact between input and refractory material occurred, avoiding corrosion completely.

This study proved that coatings and different sizes of susceptor materials for crucible protection have a high potential for future industrial applications for the InduRed reactor concept. A combination of both concepts could potentially maximize the effect of protection against diffusion. However, to close the mass balance for Lithium and other volatile elements, an optimized off-gas concept has to be elaborated in future work.

CRediT authorship contribution statement

Lukas Wiszniewski: Writing – review & editing, Writing – original draft, Visualization, Project administration, Methodology, Investigation, Conceptualization. **Zlatko Raonic:** Writing – original draft, Visualization, Supervision, Investigation. **Irmtraud Marschall:** Writing – original draft, Investigation. **Andreas Schönberg:** Writing – review & editing, Investigation. **Damaris Legenstein:** Investigation. **Klaus Doschek-Held:** Writing – review & editing.
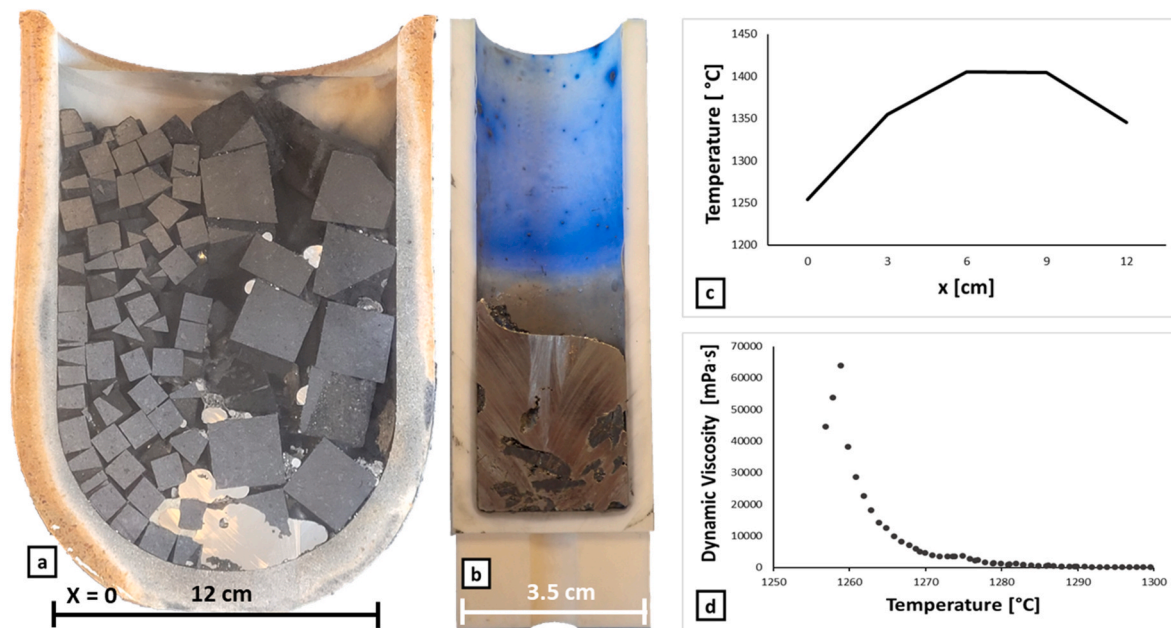
Fig. 11. Influence of a temperature gradient on crucible protection: a.) cross-section of the LCO_Ss trial with varying sizes of graphite cubes, b.) cross-section of the crucible with the alloy from the LCO_Ref trial with inclusions used for viscosity test, c.) temperature distribution within the LCO_Ss crucible after 8h of heating with a heating ramp of approximately 200 °C h^{-1}, d.) dynamic viscosity of the LCO alloy obtained from the LCO_Ref trial.

Declaration of competing interest

The authors declare the following financial interests/personal relationships which may be considered as potential competing interests: Andreas Schoenberg has patent issued to -. If there are other authors, they declare that they have no known competing financial interests or personal relationships that could have appeared to influence the work reported in this paper.

Acknowledgement

Data availability

All data used is provided within the paper

References

[1] Q. Hassan, P. Viktor, T.J. Al-Musawi, B. Mahmood Ali, S. Algburi, H.M. Alzoubi, A. Khudhair Al-Jiboory, A. Zuhair Sameen, H.M. Salman, M. Jaszczur, The renewable energy role in the global energy Transformations, Renewable Energy Focus 48 (2024) 100545, https://doi.org/10.1016/j.ref.2024.100545.

[2] A.A. Akaev, O.I. Davydova, A mathematical description of selected energy transition scenarios in the 21st century, intended to realize the main goals of the Paris climate agreement, Energies 14 (2021) 2558, https://doi.org/10.3390/en14092558.

[3] O.K. Olajiga, E.C. Ani, Z.Q. Sikhakane, T.M. Olatunde, Assessing the potential of energy storage solutions for grid efficiency: a review, Eng. sci. technol. j. 5 (2024) 1112–1124, https://doi.org/10.51594/estj.v5i3.974.

[4] O. Alšauskas, E. Connelly, M. Huismans, E. Jenness, J. Jorquera Copier, J.-B. Le Marois, T. Lombardo, S. McDonagh, V. O'Riordan, A. Petropoulos, J. Sery, Global EV Outlook 2024: Moving towards Increased Affordability, 2024.

[5] J. Zhu, I. Mathews, D. Ren, W. Li, D. Cogswell, B. Xing, T. Sedlatschek, S.N. R. Kantareddy, M. Yi, T. Gao, Y. Xia, Q. Zhou, T. Wierzbicki, M.Z. Bazant, End-of-life or second-life options for retired electric vehicle batteries, Cell Reports Physical Science 2 (2021) 100537, https://doi.org/10.1016/j.xcrp.2021.100537.

[6] M. Gutsch, J. Leker, Costs, carbon footprint, and environmental impacts of lithium-ion batteries – from cathode active material synthesis to cell manufacturing and recycling, Appl. Energy 353 (2024) 122132, https://doi.org/10.1016/j.apenergy.2023.122132.

[7] European Commission, Directorate-General for Internal Market, Industry, Entrepreneurship and SMEs, M. Grohol, C. Veeh, Study on the Critical Raw Materials for the EU 2023 – Final Report, Publications Office of the European Union, 2023.

[8] THE EUROPEAN PARLIAMENT AND THE COUNCIL OF THE EUROPEAN UNION, REGULATION (EU) 2023/1542 of the EUROPEAN PARLIAMENT and of the COUNCIL: Concerning Batteries and Waste Batteries, Amending Directive 2008/98/EC and Regulation (EU) 2019/1020 and Repealing Directive 2006/66/EC, 2023.

[9] Y.E. Milian, N. Jamett, C. Cruz, S. Herrera-León, J. Chacana-Olivares, A comprehensive review of emerging technologies for recycling spent lithium-ion batteries, Sci. Total Environ. 910 (2024) 168543, https://doi.org/10.1016/j.scitotenv.2023.168543.

[10] A. Zanoletti, E. Carena, C. Ferrara, E. Bontempi, A review of lithium-ion battery recycling: technologies, sustainability, and open issues, Batteries 10 (2024) 38, https://doi.org/10.3390/batteries10010038.

[11] L. Toro, E. Moscardini, L. Baldassari, F. Forte, I. Falcone, J. Coletta, L. Toro, A systematic review of battery recycling technologies: advances, challenges, and future prospects, Energies 16 (2023) 6571, https://doi.org/10.3390/en16186571.

[12] M. Kaya, State-of-the-art lithium-ion battery recycling technologies, Circular Economy 1 (2022) 100015, https://doi.org/10.1016/j.cec.2022.100015.

[13] A. Schönberg, H. Raupenstrauch, S. Windisch, C. Ponak, V. Mally, A. Holzer (Montanuniversität Leoben) WO 2021/175703 A1.

[14] C. Ponak, Carbo-thermal Reduction of Basic Oxygen Furnace Slags with Simultaneous Removal of Phosphorus via the Gas Phase, 2019. Dissertation, Leoben.

[15] A. Schönberg, Mathematische Modellierung metallurgischer Prozesse: Induktive Erwärmung einer Graphitschüttung, 2014.

[16] A.C. Krammer, K. Doschek-Held, F.R. Steindl, K. Weisser, C. Gatschlhofer, J. Juhart, D. Wohlmuth, C. Sorger, Valorisation of metallurgical residues via carbothermal reduction: a circular economy approach in the cement and iron and steel industry, Waste Manag. Res. (2024) 734242X241240040, https://doi.org/10.1177/0734242X241240040.

[17] S. Fashu, M. Lototskyy, M.W. Davids, L. Pickering, V. Linkov, S. Tai, T. Renheng, X. Fangming, P.V. Fursikov, B.P. Tarasov, A review on crucibles for induction melting of titanium alloys, Mater. Des. 186 (2020) 108295, https://doi.org/10.1016/j.matdes.2019.108295.

[18] S. Windisch-Kern, A. Holzer, C. Ponak, H. Raupenstrauch, Pyrometallurgical lithium-ion-battery recycling: approach to limiting lithium slagging with the InduRed reactor concept, Processes 9 (2021) 84, https://doi.org/10.3390/pr9010084.

[19] A. Holzer, L. Wiszniewski, S. Windisch-Kern, H. Raupenstrauch, Optimization of a pyrometallurgical process to efficiently recover valuable metals from commercially used lithium-ion battery cathode materials LCO, NCA, NMC622, and LFP, Metals 12 (2022) 1642, https://doi.org/10.3390/met12101642.

[20] L. Wiszniewski, I. Marschall, T. Hochsteiner, T. McFarlane Hoad, K. Doschek-Held, H. Raupenstrauch, Evaluating refractory material performance in pyrometallurgical recycling of lithium-ion batteries under a reducing atmosphere, Ceram. Int. (2024), https://doi.org/10.1016/j.ceramint.2024.08.220.

[21] N. Nayan, Govind, C.N. Saikrishna, K.V. Ramaiah, S.K. Bhaumik, K.S. Nair, M.C. Mittal, Vacuum induction melting of NiTi shape memory alloys in graphite crucible, Mater. Sci. Eng., A 465 (2007) 44–48, https://doi.org/10.1016/j.msea.2007.04.039.

[22] Z. Zhang, J. Frenzel, K. Neuking, G. Eggeler, Vacuum induction melting of ternary NiTiX (X=Cu, Fe, Hf, Zr) shape memory alloys using graphite crucibles, Mater. Trans. 47 (2006) 661–669, https://doi.org/10.2320/matertrans.47.661.

[23] T. Bello, E. Dung, S. Musa, E. Wuritka, A. Tokan, Potentials of Graphite as a Material for the Production of Crucibles, 2023.

[24] F. Wolny, A. Krause, M. Müller, G. Fischer, H. Neuhaus, Reduced metal contamination from crucible and coating using a silicon nitride based diffusion barrier for the growth of cast quasi-single crystalline silicon ingots, J. Cryst. Growth 514 (2019) 49–53, https://doi.org/10.1016/j.jcrysgro.2019.02.055.

[25] A. Mohanty, D.K. Patel, S.K. Panigrahi, Susceptor based design strategies for enhancing microwave hybrid heating capability via experimental analysis, 3D multi-physics simulation and parametric optimization, Int. J. Therm. Sci. 196 (2024) 108674, https://doi.org/10.1016/j.ijthermalsci.2023.108674.

[26] J.S. Park, H. Shimada, S. Taniguchi, K. Betsumori, H. Morino, S. Yamada, Numerical calculation of Joule heat generated by susceptor heating with induction for waste vitrification, Trans. Mat. Res. Soc. Japan 32 (2007) 615–618, https://doi.org/10.14723/tmrsj.32.615.

[27] A. Holzer, S. Windisch-Kern, C. Ponak, H. Raupenstrauch, A novel pyrometallurgical recycling process for lithium-ion batteries and its application to the recycling of LCO and LFP, Metals 11 (2021) 149, https://doi.org/10.3390/met11010149.

[28] C. Wilke, A. Kaas, U.A. Peuker, Influence of the cell type on yield and composition of black mass deriving from a mechanical recycling process of automotive Lithium-ion batteries, Sustainability 4 (2024) 100050, https://doi.org/10.1016/j.nxsust.2024.100050.

[29] L. Wiszniewski, C. Gatschlhofer, A. Krammer, T. Hochsteiner, A. Holzer, H. Raupenstrauch, Influences of Pre-treatment Steps and Contaminants in a Pyrometallurgical Recycling Process for NCA (LiNi0.8Co0.15Al0.05O2) Lithium-Ion Battery Material, Livingstone, Sambia, 2023.

[30] Damaris Legenstein, Entwicklung eines Multi-Region-Simulationsmodells und eines Reaktionskinetik-Ansatzes auf Basis des InduRed-Reaktors, Master Thesis, Leoben, 2021.

[31] H. Joubert, Designing for Slag "Freeze Linings" on Furnace Sidewalls – an Engineering Perspective, South africa.

[32] D. Gregurek, J. Schmidl, K. Reinharter, C. Majcenovic, A. Spanring, S. Schmidt, J. Böhlke, Customized refractory solutions to deal with increasing complexity in copper recycling, RHI Bulletin - The journal of refratory innovations (2020).

[33] S. Hla, The effect of solids and phase compositions on viscosity behaviour and TCV of slags from Australian bituminous coals, J. Non-Cryst. Solids (2011).

[34] I. Bellemans, J. Zietsman, K. Verbeken, Fundamental and formation aspects of slag freeze linings: a review, J. Sustain. Metall. 8 (2022) 64–90, https://doi.org/10.1007/s40831-022-00505-z.

[35] T. Crivitis, Fundamental Studies on the Chemical Aspects of Freeze Linings, Dissertation, Queensland, Australia, 2016.

[36] P. Duncanson, J. Toth, The Truths and Myths of Freeze Lining Technology for Submerged Arc Furnaces, Columbia, Tennessee, USA, 2004.

[37] B.A. Nuraeni, K. Avarmaa, L.H. Prentice, W.J. Rankin, M.A. Rhamdhani, Recovery of cobalt and lithium by carbothermic reduction of LiCoO2 cathode material: a kinetic study, Metall. Mater. Trans. B 54 (2023) 602–620, https://doi.org/10.1007/s11663-022-02712-1.

[38] R.K. Wunderlich, H.-J. Fecht, G. Lohöfer, Surface tension and viscosity of the Ni-based superalloys LEK94 and CMSX-10 measured by the oscillating drop method on board a parabolic flight, Metall. Mater. Trans. B 48 (2017) 237–246, https://doi.org/10.1007/s11663-016-0847-y.

[39] A. Yakymovych, Y. Plevachuk, S. Mudry, J. Brillo, H. Kobatake, H. Ipser, Viscosity of liquid Co-Sn alloys: thermodynamic evaluation and experiment, Phys. Chem. Liq. 52 (2014) 562–570, https://doi.org/10.1080/00319104.2013.876639.